Inorganic Chemistry
Article
pubs.acs.org/IC

P2-$Na_xMn_{1/2}Fe_{1/2}O_2$ Phase Used as Positive Electrode in Na Batteries: Structural Changes Induced by the Electrochemical (De)intercalation Process

Benoit Mortemard de Boisse,[†] Dany Carlier,*[,†] Marie Guignard,[†] Lydie Bourgeois,[‡] and Claude Delmas[†]

[†]CNRS, Université de Bordeaux, ICMCB, 33608 Pessac Cedex, France

[‡]Université de Bordeaux, CNRS, ISM, Groupe Spectroscopie Moléculaire, 33405 Talence Cedex, France

Supporting Information

ABSTRACT: The electrochemical properties of the P2-type $Na_xMn_{1/2}Fe_{1/2}O_2$ ($x = 0.62$) phase used as a positive electrode in Na batteries were tested in various voltage ranges at C/20. We show that, even if the highest capacity is obtained for the first cycles between 1.5 and 4.3 V, the best capacity after 50 cycles is obtained while cycling between 1.5 and 4.0 V (120 mAh g^{-1}). The structural changes occurring in the material during the (de)intercalation were studied by operando in situ X-ray powder diffraction (XRPD) and ex situ synchrotron XRPD. We show that a phase with an orthorhombic P′2-type structure is formed for $x \approx 1$, due to the cooperative Jahn–Teller effect of the Mn^{3+} ions. P2 structure type stacking is observed for $0.35 < x < 0.82$, while above 4.0 V, a new phase appears. A full indexation of the XRPD pattern of this latter phase was not possible because of the broadening of the diffraction peaks. However, a much shorter interslab distance was found that may imply a gliding of the MO_2 slab occurring at high voltage. Raman spectroscopy was used as a local probe and showed that in this new phase the MO_2 layers are maintained, but the phase exhibits a strong degree of disorder.

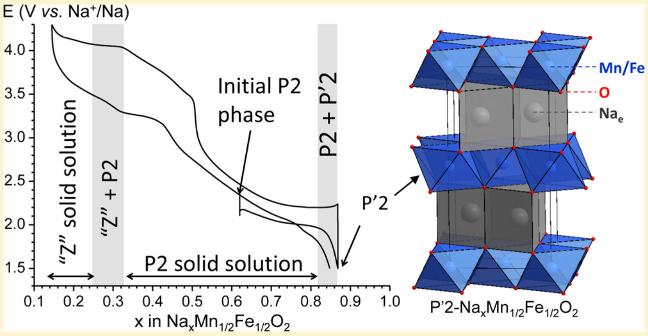

■ INTRODUCTION

In the past few years there has been a renewed interest in sodium layered oxides for use as positive electrodes in sodium ion batteries.[1] A great number of them are Mn and/or Fe based, since these elements are abundant and nontoxic: Na_xFeO_2,[2] $Na_x(Mn,Fe)O_2$,[3] $Na_x(Ni,Fe,Mn)O_2$,[4] $Na_x(Ni,Mn,Co)O_2$.[5] Due to the larger ionic radius of the Na^+ ion in comparison to the Li^+ ion (1.02 Å vs 0.76 Å) and its ability to be either in octahedral or in trigonal-prismatic environments, several Na_xMO_2 polytypes can be obtained, depending on the Na/M ratio and on the synthesis conditions. In the alkali layered oxide designation, these phases are described by a letter, indicating the site geometry of the alkali ion (prismatic (P) or octahedral (O)) followed by a number, corresponding to the number of MO_2 slabs needed to describe the hexagonal cell (2 or 3 typically).[6] Two types of phases, obtained by direct synthesis and showing interesting Na ion (de)intercalation properties, have been reported in the $Na_xMn_{1-y}Fe_yO_2$ system so far: P2 and O3. In our previous work we compared the electrochemical properties for the P2- and O3-$Na_xMn_{1/2}Fe_{1/2}O_2$ phases among other materials and confirmed that the P2 phases exhibit a high reversible capacity.[3d] According to Yabuuchi et al.,[3a] they are better candidates for Na ion batteries. In this work, we focus on the P2-$Na_xMn_{1/2}Fe_{1/2}O_2$ phase and study the structural changes occurring during cycling by in situ X-ray powder diffraction (in situ XRPD), synchrotron X-ray powder diffraction (SXRPD), and Raman spectroscopy.

■ EXPERIMENTAL SECTION

The synthesis protocol of the P2-$Na_xMn_{1/2}Fe_{1/2}O_2$ phase is described in detail in our previous work.[3d] Manganese, iron, and sodium nitrates were dissolved along with glycine in deionized water. The targeted phase was P2-$Na_{0.67}Mn_{1/2}Fe_{1/2}O_2$. A sodium excess of 10 wt % was used to take into account the high volatility of sodium oxides during the subsequent heat treatment. The mixture was then heated in a ceramic bowl placed in a sand bath ($T \approx 400$ °C). The product from the combustion reaction was then ground and heated to 700 °C in air for 20 h and at 1000 °C under O_2 for 5 h. After the heat treatment, the powder was quenched to room temperature and introduced into an Ar-filled glovebox to avoid oxidation and reaction with air moisture. The sodium content was confirmed by induced coupled plasma-atomic emission spectroscopy analysis and Rietveld refinement of the structure, on the basis of the X-ray powder diffraction (XRPD) pattern.

The synchrotron X-ray powder diffraction (SXRPD) pattern of the starting material was recorded at the Argonne Photon Source (APS, Argonne National Laboratory, Argonne, IL, USA) at a high-resolution powder diffraction beamline (11-BM). The powder was loaded into a 1.5 mm diameter Kapton capillary sealed with epoxy. The wavelength used was equal to 0.413913 Å. All data were recorded three times

Received: July 24, 2014
Published: September 25, 2014

dx.doi.org/10.1021/ic5017802 | *Inorg. Chem.* 2014, 53, 11197−11205

between 0 and 60° (2*θ* range) (~50 min/pattern) and then merged with a 0.002° step size. The Rietveld refinement of the structure was performed from SXRPD patterns recorded between 0 and 60°, though we chose to show only the range corresponding to 10−70° (2*θ* Cu Kα_1) in the present paper.

The SXRPD pattern of the discharged material was recorded at the European Synchrotron Radiation Facility (ESRF, Grenoble, France) at the high-resolution powder diffraction ID31 beamline. The powder was loaded into a 1 mm diameter glass capillary sealed with epoxy. The wavelength used was equal to 0.399845 Å. The data were recorded twice between 0 and 44° (2*θ* range) (~27 min/pattern) and then merged with a 0.002° step size. The Rietveld refinement of the structure was performed from SXRPD patterns recorded 2 and 40°, though we chose to show only the range corresponding to 10−70° (2*θ* Cu Kα_1) in the present paper.

The electrochemical characterizations were carried out in Na/electrolyte/$Na_xMn_{1/2}Fe_{1/2}O_2$ batteries assembled in 2032 type coin cells. The positive electrode consisted of an active material/carbon black (CB)/polytetrafluoroethylene mixture in a 77/17/6 weight ratio (total mass ~22 mg). The electrolyte was obtained by dissolution of $NaPF_6$ (Alpha Aesar 99+%) in propylene carbonate (PC, Sigma-Aldrich anhydrous 99%) to reach a concentration of 1 mol L^{-1}. Fluoroethylene carbonate (FEC, 2 wt %; obtained through an industrial partner) was added to the electrolyte to limit its decomposition at high voltage.[7] All data were recorded using a Biologic VMP3 potentiostat. The electrodes were separated by three layers of Whatman glass fiber sheets.

Operando in situ XRPD was carried out using an in situ cell purchased from the LRCS, Amiens, France,[8] on a Bruker D5000 diffractometer equipped with a Cu target. After a preliminary experiment, the 13−20 and 30−43° 2*θ* ranges were selected for the acquisitions during cycling. The electrochemical cell is similar to that described above, and the cell was previously fully discharged and placed under constant voltage at 1.5 V vs Na^+/Na before recording the full charging process. We therefore started the experiment from a material with the highest intercalated Na amount. The current rate was approximately *C*/100, and the XRPD pattern was recorded every $\Delta x_{Na} = 0.01$. The electrochemical data were controlled and recorded using a Biologic VMP3 potentiostat.

All of the voltages mentioned in the present paper are expressed versus the Na^+/Na redox couple.

Raman scattering measurements were performed with a Jobin Yvon Horiba Labram HR-800 microspectrometer. The spectra were recorded using a 514 nm excitation wavelength of an Ar^+ laser, with the power adjusted to 100 *μ*W in order to avoid any degradation of the sample. Specifically designed airtight cells were used in order to keep the sample under Ar.

■ RESULTS AND DISCUSSION

Structural Study of the Pristine Material. In previous work, we reported the structure of the pristine P2-$Na_xMn_{1/2}Fe_{1/2}O_2$ phase on the basis of laboratory XRPD data. Unfortunately, we could not refine properly the atomic displacement parameters (ADPs) of the different ions. In the present work, we present synchrotron XRPD (SXRPD) analysis that leads to a better description of the structure of the starting material. The experimental SXRPD pattern and the calculated pattern resulting from the structural Rietveld refinement using a pseudo-Voigt profile are shown in Figure 1. The refined cell and atomic parameters are reported in Table 1. The pattern can be refined in the hexagonal *P*6$_3$/*mmc* space group, as expected for a P2-type phase. The refined cell parameters (a_{hex} = 2.9405(1) Å and c_{hex} = 11.1957(2) Å) are very close to those determined in our previous work on another batch of the P2-$Na_xMn_{1/2}Fe_{1/2}O_2$ material[3d] and in the literature.[3a,e] The very low signal/noise ratio allows us to refine the occupation of the different Na sites along with the different isotropic ADPs. The

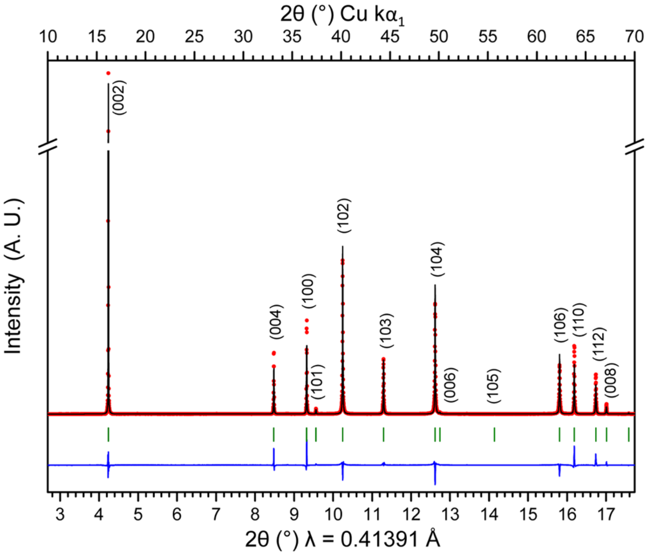

Figure 1. Observed and calculated (Rietveld method) synchrotron X-ray powder diffraction pattern for the P2-$Na_{0.62}Mn_{1/2}Fe_{1/2}O_2$ starting phase: (red dots) experimental data; (black line) calculated data; (blue line) difference; (green bars) Bragg positions.

Table 1. Cell and Atomic Parameters and Reliability Factors Calculated from the Synchrotron Diffraction Powder Pattern of the P2-$Na_{0.62}Mn_{1/2}Fe_{1/2}O_2$ Starting Phase[a]

		coordinates				
atom	Wyckoff	*x*	*y*	*z*	occ.	ADP (Å^2)
Na(1)	2d	0	0	1/4	0.18(1)	1.8(7)
Na(2)	2b	2/3	1/3	1/4	0.44(2)	1.9(4)
Mn	2a	0	0	0	1	0.29(3)
Fe	2a	0	0	0		
O	4f	1/3	2/3	0.0930(6)	1	0.7(1)

distances (Å)	
M−O	Na−O
6 × 1.99(1)	6 × 2.44(1)

[a] Space group: *P*6$_3$/*mmc*. a_{hex} = 2.9405(1) Å, c_{hex} = 11.1957(2) Å. R_{wp} =15.33%; R_B = 8.93%.

overall sodium content is equal to 0.62(3), which is in good agreement with the targeted composition ($Na_{0.67}Mn_{1/2}Fe_{1/2}O_2$) and that determined by ICP-AES analysis ($Na_{0.66(2)}Mn_{0.47(2)}Fe_{0.53(2)}O_2$). The associated ADPs are equal to 1.8(7) and 1.9(4) Å^2 for the two sodium sites (2d and 2b), respectively, which is high but usual for Na_xMO_2 materials with $x < 1$.[5f,9] This may result from the high mobility of sodium in layered phases. Occupancies of the transition metal and oxygen sites were fixed to 1, and the associated ADPs show the more usual values of 0.29(3) Å^2 (Fe and Mn in 2a site) and 0.7(1) Å^2 (O in 4f site). We also tried to refine the transition-metal site occupancy, as we suggested that some transition-metal vacancies could occur[3d] by comparison to previous work on P2-$Na_{0.7}MnO_2$.[10] However, any attempt to include transition-metal vacancies in the MO_2 slabs did not lead to significant improvement of the refinement. Because of the 1:1 ratio between the Mn and Fe atoms which can induce a transition-metal ordering, we carried out neutron diffraction experiments at the D2B high-resolution powder diffractometer at the Insitut Laue-Langevin (ILL, Grenoble, France). However, no evidence of Mn/Fe ordering in the MO_2 layers was observed.

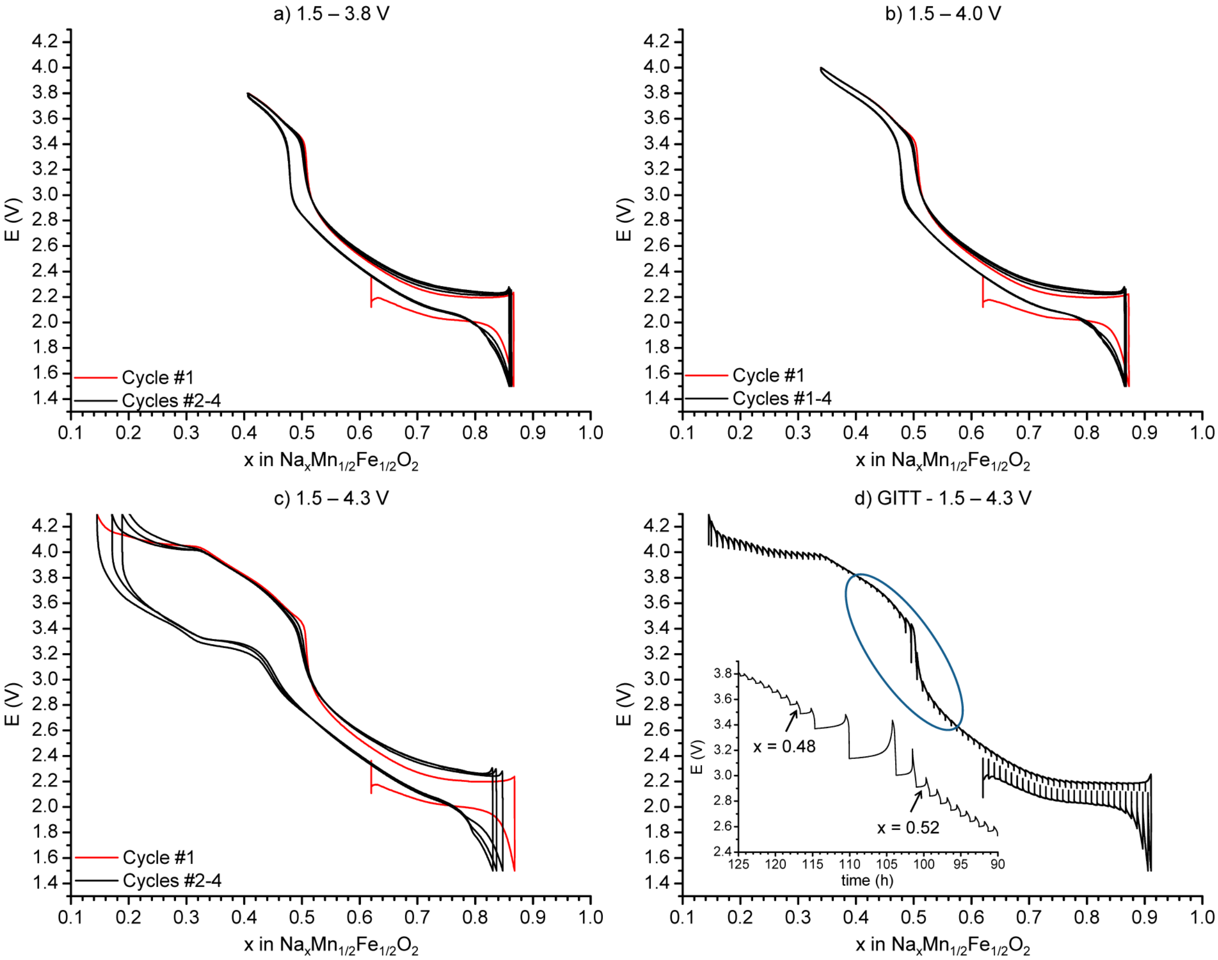

Figure 2. (a−c) Galvanostatic cycling curves recorded at C/20 rate between (a) 1.5 and 3.8 V, (b) 1.5 and 4.0 V and (c) 1.5 and 4.3 V. (d) GITT curve recorded with steps of ∼0.01 Na^+ per formula unit and the relaxation condition dE/dt < 4 mV h^{-1}.

Electrochemical Characterizations. In order to have a better understanding of the performances and limitations of P2-$Na_xMn_{1/2}Fe_{1/2}O_2$ as a positive electrode material for Na ion batteries, we carried out several electrochemical experiments with various upper voltage cutoffs. The galvanostatic curves (Figure 2) show the evolution of the cell voltage as a function of the sodium content using a C/20 cycling rate in the following voltage ranges: 1.5−3.8 V (a), 1.5−4.0 V (b), and 1.5−4.3 V (c). The shapes of the $E = f(x)$ curves are similar to those reported in the literature for the 1.5−3.8 and 1.5−4.0 V ranges[3a] (Figure 2a,b): during the initial discharge from P2-$Na_{0.62}Mn_{1/2}Fe_{1/2}O_2$, a short voltage plateau at ∼2.05 V is observed, suggesting that a phase transition is occurring at the end of the discharge. During Na deintercalation, the same plateau is observed at ∼2.2 V (thus reversible). Upon further deintercalation, the $E = f(x)$ curves exhibit a solid solution behavior and undergo a sudden voltage jump at $x \approx 0.5$. Note that the first cycle is always slightly different from the following cycles for each upper voltage cutoff. From the second cycle the cycling process is reversible and the cells exhibit quite a low polarization when cycled up to 3.8 or 4.0 V. When the upper cutoff voltage is increased to 4.3 V, a second plateau is observed at approximately 4.0 V. During the following discharge, this plateau is no longer visible and instead an important increase of the polarization is observed. Then, once the cell voltage reaches 3.2 V during discharge, the process seems again fully reversible. To get more insight into the reversibility of this process, another experiment was done: after three cycles in the range 1.5−4.3 V, range the upper voltage limit was reduced to 4.0 V. As shown in Figure 3, the shape of the curve is similar to that obtained directly using the same voltage range (Figure 2b). This result shows that the structural modification occurring

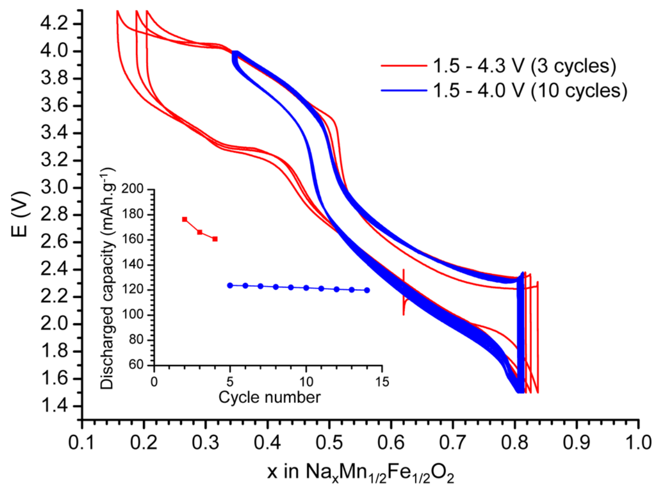

Figure 3. Galvanostatic curves recorded at a C/20 rate between 1.5 and 4.3 V (in red) and then between 1.5 and 4.0 V (in blue). The insert represents the evolution of the associated discharge capacities.

above 4.0 V is completely reversible. Moreover, it shows that a significant amount of sodium has to be reintercalated to induce the reversible phase transition. The large polarization and the large hysteresis of the process show that a great deal of energy is involved.

To get a better understanding of the behavior of this system, we carried out a galvanostatic intermittent titration technique (GITT) experiment, reported in Figure 2d, which allows characterizing the material in its relaxed state. The shape of the obtained GITT curve is similar to those of the galvanostatic experiments, and it exhibits a first plateau at 2.1 V for $0.82 \leq x \leq 0.90$. Upon charging, we observe a continuous decrease of the polarization until $x = 0.52$ ($\Delta E = 74$ mV at $x = 0.52$). For $x \leq 0.48$ the polarization is very low ($\Delta E = 42$ mV for $x = 0.48$) down to $x = 0.33$ (4.0 V), as shown in the inset of Figure 2d. Upon further deintercalation, a second plateau is observed at ~4.0 V for $0.25 < x < 0.33$. On this plateau the polarization continuously increases along with the voltage up to 4.3 V. Considering the relative position of the Fe^{3+}/Fe^{4+} and Mn^{3+}/Mn^{4+} redox couples in oxides, one can assume the following classical distribution of cations in the starting material: $Na_{0.62}Mn^{4+}{}_{0.38}Mn^{3+}{}_{0.12}Fe^{3+}{}_{0.50}O_2$. During the first discharge almost all Mn^{4+} ions are reduced to the trivalent state and then they are reoxidized during the first charge. The rapid cell voltage increase for $x = 0.50$ suggests that trivalent manganese ions are oxidized for $0.50 \leq x \leq 1.0$ and then trivalent iron ions for $x < 0.50$. As shown in the inset of Figure 2d, the polarizations are very different on both sides of the $x = 0.5$ composition which can be related to the electronic transfer between the involved cations. For $x > 0.5$ Mn^{3+}/Mn^{4+} hopping is involved, while the Fe^{3+}/Fe^{4+} couple is only active for $x < 0.50$. The change in polarization is due to the easier electronic transfer in the case of the iron couple. Moreover, for $x = 0.5$ the polarization is quite high because, at this exact composition, there are only Mn^{4+} and Fe^{3+} in the material, which prevents an easy electronic transfer.

We then investigated the importance of the upper cutoff voltage on the long-term electrochemical cycling, as reported in Figure 4. If the cutoff voltage is set to 3.8 V (Figure 4a) or 4.0 V (Figure 4b), the 25th and 50th cycles do not show any significant evolution in comparison to the first cycle (the initial discharge is not considered) followed by the second discharge, in addition to a progressive decrease of the capacity and a small increase of the polarization. On the other hand, if the cutoff voltage is set to 4.3 V (Figure 4c), the shape of the cycling curve exhibits drastic evolutions upon cycling: (i) the polarization of the curve increases, (ii) a smoothing of the voltage jump at $x = 0.5$ is observed, and (iii) the second plateau observed at ~3.3 V in discharge decreases in length (x) at the 25th cycle and disappears at the 50th cycle. These changes in behavior result in a strong decrease of the capacity upon cycling: while 0.70 Na^+ ion per formula unit is reintercalated between the first charge and the second discharge, only 0.52 and 0.44 Na^+ ion is reversibly cycled in the 25th and 50th cycles, respectively. In Figure 4d, we plot the evolution of the discharged capacity along with the cycle number for the different cutoff voltages used. Whereas the second discharged capacities increase with the upper cutoff voltage (120, 140, and 185 mAh g^{-1}, respectively, for $E_{cutoff} = 3.8$, 4.0, 4.3 V), the capacity retention at the 50th cycle is inversely proportional (91%, 85%, and 60% retention for $E_{cutoff} = 3.8$, 4.0, and 4.3 V, respectively). One can observe that using a high 4.3 V cutoff voltage does not lead to a capacity improvement for long-term cycling, since after about 40 cycles the capacity value of the cells with $E_{cutoff} = 4.0$ V is reached (125 mAh g^{-1}).

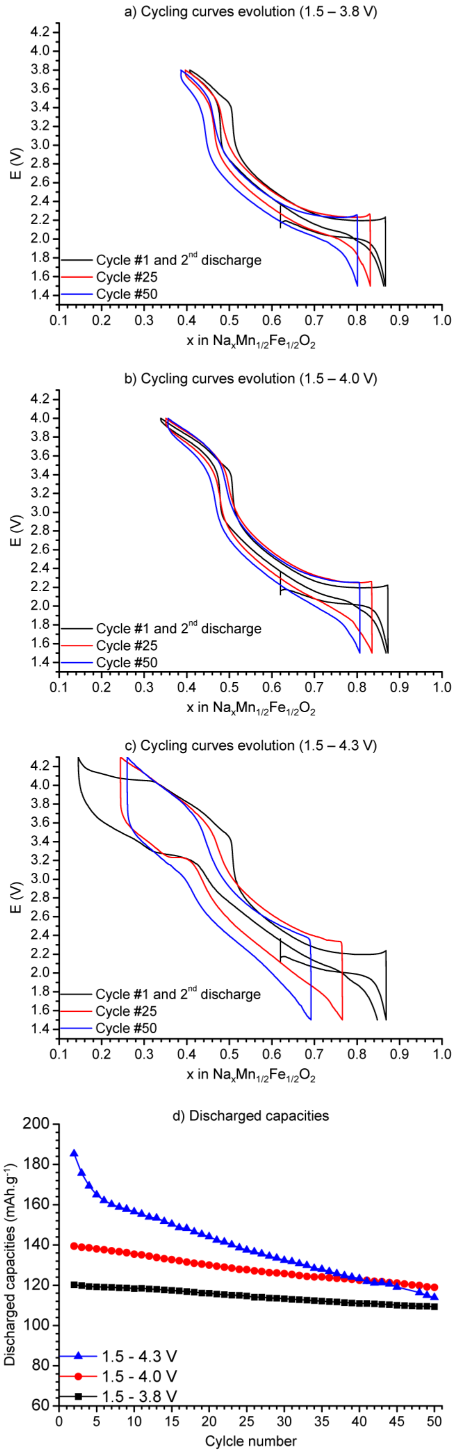

Figure 4. (a–c) Comparison of the first cycle + second discharge, 25th and 50th cycles, for the experiments carried out in the (a) 1.5–3.8 V, (b) 1.5–4.0 V, and (c) 1.5–4.3 V ranges. (d) Evolution of the discharge capacities corresponding to the galvanostatic cycling curves presented in Figure 2a–c.

In Situ XRPD Study. To study the structural rearrangements occurring upon cycling in the material, we carried out an operando in situ XRPD experiment. The evolution of the XRPD patterns along with the complete charge of the battery is showed in Figure 5 and Figure S1 (Supporting Information) in

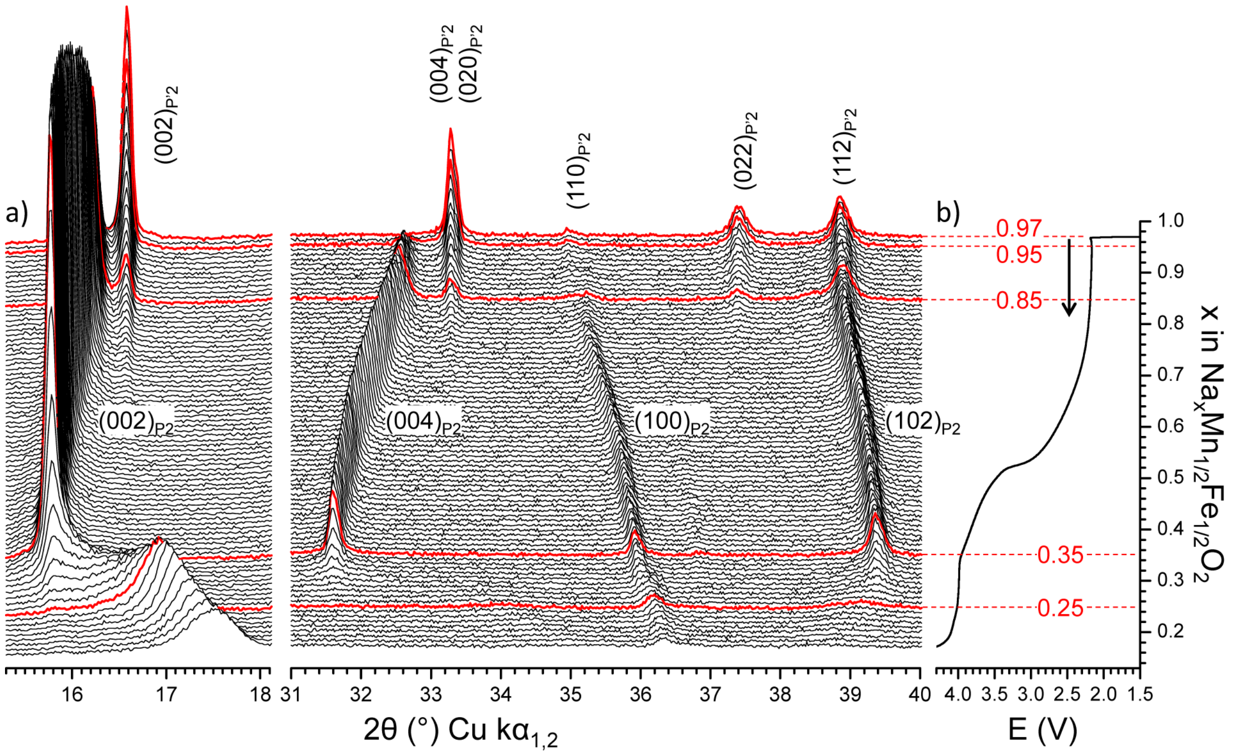

Figure 5. (a) Operando in situ XRPD patterns of the $Na_xMn_{1/2}Fe_{1/2}O_2$ electrode material, recorded during the complete charge of a $Na_xMn_{1/2}Fe_{1/2}O_2/NaPF_6$ in PC (1 M) + 2 wt % FEC/Na cell. (b) The corresponding cycling curve. The red XRPD patterns correspond to the limits of the different structural domains.

reverse order. The experiment starts from the material in the fully discharged state, which corresponds to the composition $Na_{0.97}Mn_{1/2}Fe_{1/2}O_2$. In its diffraction pattern, two diffraction peaks—observed at approximately 37.4 and 38.8°—cannot be indexed using the hexagonal symmetry of the pristine material. Instead, an orthorhombic cell should be used to index the pattern as for P′2-$Na_{0.7}MnO_2$.[11] According to the structural classification of Na_xMO_2 phases, we will refer to this phase as a P′2-type structure.[6] Therefore, these two diffraction peaks correspond respectively to the $(022)_{P'2}$ and $(112)_{P'2}$ reflections in the orthorhombic symmetry and arise from the splitting of the $(102)_{P2}$ reflection in the hexagonal symmetry. The P′2-type structure is observed as a single phase only for a narrow Na range of $0.95 < x \leq 0.97$. For $x \leq 0.95$, a second phase is formed (Figure S1). It is clearly visible with the appearance of two diffraction peaks at approximately 16.3 and 32.6° that correspond to the $(002)_{P2}$ and $(004)_{P2}$ reflections in the hexagonal cell (P2-type structure), respectively. The biphasic domain between the P2 and P′2 phases is observed for a Na content of $0.85 < x \leq 0.95$.

Upon further charging, only a single phase with P2-type structure is present down to $x \approx 0.35$. For $0.25 < x \leq 0.35$, a new biphasic domain is observed with the appearance of very broad diffraction peaks, which appear at approximately 16.8 and 36.1°. The continuous displacement of this first diffraction reflection upon Na deintercalation shows that the biphasic domain, consisting of a mixing of the P2 phase and a new material appearing for $x \approx 0.25$, is actually a solid solution. For $x < 0.25$, the diffraction lines become even broader, indicating a loss in long-range order with an asymmetry of the (002) line on the high 2θ angle side (Figure 5). An indexation of the XRPD diagram at the end of charging was not possible because only two diffraction peaks were observed. However, we suspect that the MO_2 layers glided upon sodium deintercalation, imposing an octahedral environment for sodium ions, as was suggested by several authors.[3a,12] Therefore, as we do not have any data for the packing type, we will refer to this deintercalated phase as the "Z phase".

After the operando in situ XRPD experiment and the charging up to 4.3 V, the cell was discharged again down to 1.5 V and maintained at this voltage until a negligible residual current was observed. The XRPD pattern recorded after this second discharge is comparable to that recorded after the first discharge in Figure 6. As suggested by the cycling curve reported in Figure 3, the XRPD pattern after the second

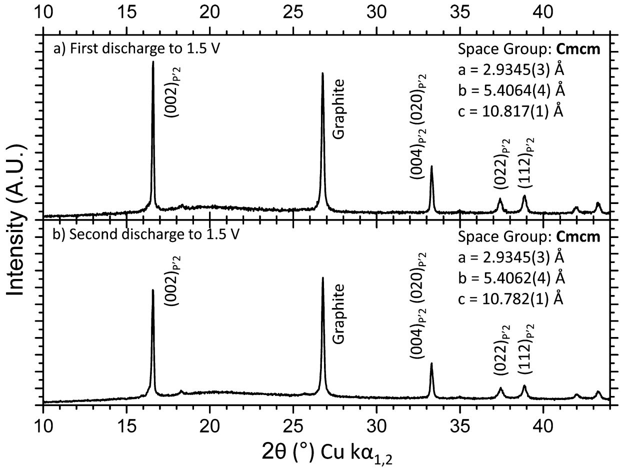

Figure 6. Comparison of the patterns recorded for the phases obtained after the first (a) and second discharges (b) at 1.5 V and maintained at the voltage until negligible current is observed.

discharge is again characteristic of a well-crystallized phase, with well-defined diffraction peaks, which confirms that sodium electrochemical intercalation is still very reversible even after the charge up to high voltage. Both patterns are indexed in an orthorhombic cell, and they have very close cell parameters. The pattern corresponding to the second discharge (Figure 6b) exhibits slightly broader diffraction peaks, probably resulting from the decrease of the diffraction coherent length due to the electrochemical grinding of the material upon cycling to 4.3 V. Nevertheless, as the capacities after 50 cycles are almost the same for all cycling conditions, we have no explanation for the capacity loss or for the mechanism involved at high voltage.

Two characteristic distances of layered oxide structures can be deduced from the indexation of the XRPD patterns recorded during the in situ experiment. The first is the interslab distance, which is the distance between two successive MO_2 layers, while the second one is the in-plane M−M distance. For both phases with P′2- and P2-type structures, the interslab distance is equal to half the *c* parameter.

For the P2-type phase, there is only one in-plane M−M distance, equal to the a_{hex} parameter, whereas for the P′2-type phase, two different in-plane M-M distances can be found: one is equal to the a_{orth} parameter, and one is equal to $((a_{orth}^2 + b_{orth}^2)/2)^{1/2}$. The variation of the interslab distance is reported in Figure 7a, while the variations of the a_{hex}, a_{orth}, and b_{orth} cell parameters are reported in Figure 7b. The main feature concerns the interslab distance, which increases continuously for the P2 type and then decreases when the “Z” phase is formed.

Concerning the “Z” phase appearing at high voltage, for which the XRPD pattern could not be indexed, only two diffraction lines are seen on the XRPD patterns. As they are very close to the $(002)_{P2}$ and $(100)_{P2}$ patterns, one can assume that this material presents for the $x = 0.25$ composition an interslab distance of 5.3 Å and an in-plane M−M distance equal to 2.88 Å. The absence of well-defined diffraction lines shows that there is no long-range ordering in the MO_2 slab packing.

For a very general point of view, when the number of alkali ions in the interslab space is very small, the covalence of the bonds in the MO_2 slab increases thanks to the transition-metal oxidation. This leads to a decrease of the interslab thickness. In the case of P2-type phases this decrease will increase the repulsions between the oxygen layers of the NaO_6 trigonal prism, which is then strongly destabilized. To accommodate this interslab thickness contraction and to decrease the O−O repulsions, a shift of the slab occurs with the formation of octahedral sites in the interslab space. Upon deintercalation, the M−M distance decreases continuously as a result of the transition-metal oxidation.

The second important feature concerns the P′2-type phase and is highlighted by two distinct in-plane M−M distances of approximately 2.93 and 3.07 Å (Figure 7b). This huge difference in distance implies that the triangular lattice formed by Mn and Fe atoms is highly distorted.

Synchrotron X-ray Powder Diffraction of the P′2-Type Phase. To understand the origin of the distortion of the triangular lattice, we characterized the structure of the P′2-type phase in detail using high-resolution powder diffraction. We prepared the material by discharging a battery for which the positive electrode was made of a pellet of P2-$Na_{0.62}Mn_{1/2}Fe_{1/2}O_2$ and carbon black (80:20 in weight) down to 1.5 V. A synchrotron X-ray powder diffraction (SXRPD) experiment was performed on the positive electrode material after the discharge. The experimental SXRPD diagram and the calculated diagram resulting from the structural Rietveld refinement method are shown in Figure 8. The SXRPD pattern was successfully indexed in the *Cmcm* orthorhombic space group by analogy to other A_xMO_2 phases (A = Na, K), as we have previously mentioned.[10,11,13] The cell and atomic parameters obtained from the Rietveld refinement are reported in Table 2. The refined Na content is equal to 1.0(2), which is in agreement with that obtained from electrochemical characterizations. The b/a ratio (1.84) shows the distortion vs the ideal undistorted phase ($b/a = 1.732$ for an undistorted hexagonal phase described in an orthorhombic cell). The Rietveld refinement highlights the distortion of the MO_6 octahedra with four short M−O distances (1.99(6) Å) and two long distances (2.18(1) Å) (Table 2 and Figure 9). This distortion results from a cooperative Jahn−Teller effect, even if only half of the transition metal ions are Jahn−Teller active ions (Mn^{3+} ions). Nevertheless, one can notice that this distortion is lower than that in O′3-$NaMnO_2$, in which all transition-metal ions are Mn^{3+} ($b_{mon}/a_{mon} = 1.99$[14]). In this phase, the short Mn−O distances were found to be close to 1.94 Å and the long distance close to 2.39 Å.[14] The moderate distortion in the P′2-$Na_1Mn_{1/2}Fe_{1/2}O_2$ phase results from the presence of 0.5 Fe^{3+} ion, which is not Jahn −Teller active.

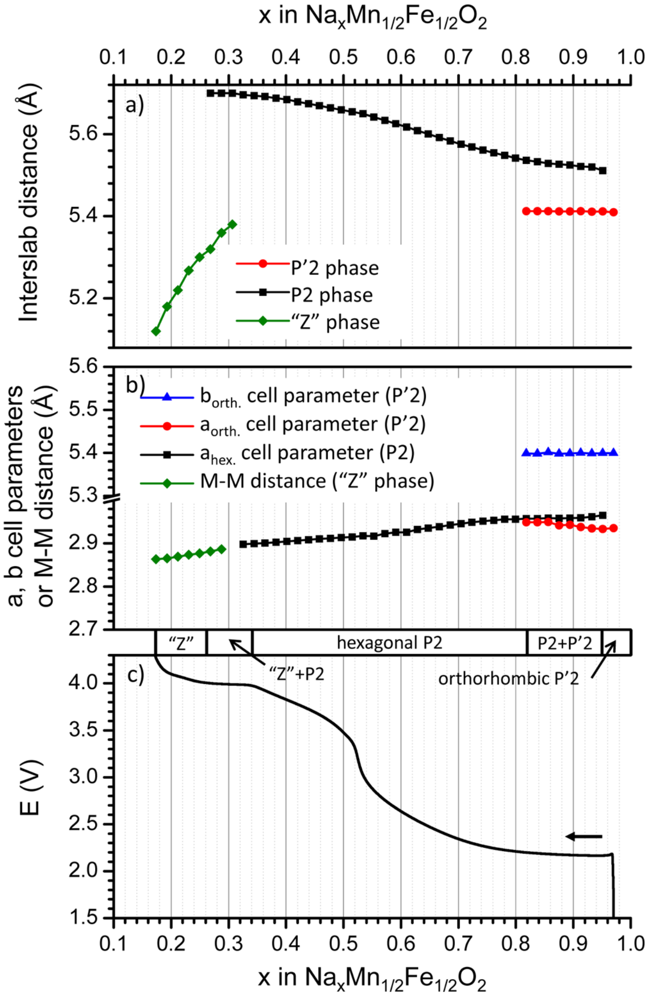

Figure 7. Evolution of (a) the interslab distance and (b) the *a* and *b* cell parameters of the P′2, P2, and “Z” phases upon sodium deintercalation. The galvanostatic curve versus *x* is also shown for more clarity in (c).

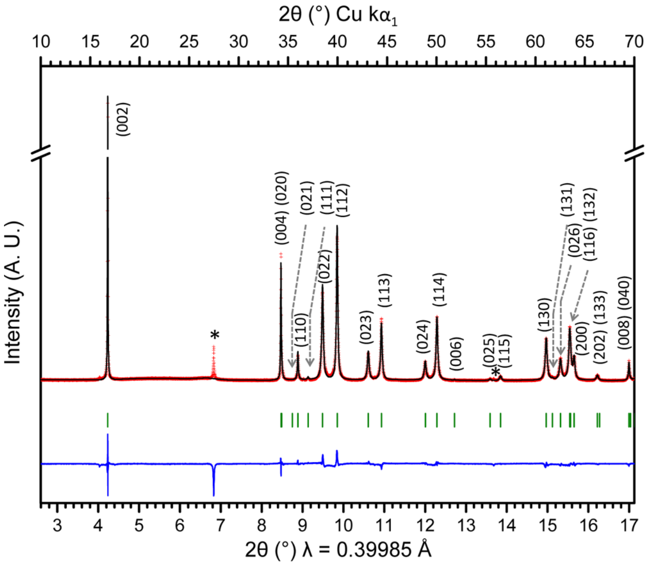

Figure 8. Observed and calculated (Rietveld method) synchrotron diffraction patterns of the P′2-$NaMn_{1/2}Fe_{1/2}O_2$ phase; (red crosses) experimental data; (black line) calculated data; (blue line) difference; (green bars) Bragg positions. Asterisks indicate graphite main diffraction lines.

Table 2. Cell and Atomic Parameters and Reliability Factors Calculated from the Synchrotron Diffraction Powder Pattern of P′2-$NaMn_{1/2}Fe_{1/2}O_2$[a]

		coordinates				
atom	Wyckoff	x	y	z	occ.	ADP (Å^2)
Na_e	4c	0	0.683(2)	1/4	1.0(2)	0.7(2)
Mn	4a	0	0	0	1	0.60(5)
Fe	4a	0	0	0		
O	8f	0	0.648(2)	0.901(1)	1	0.5(2)

distances (Å)	
M−O	Na−O
4 × 1.99(1)	4 × 2.38(1)
2 × 2.18(1)	2 × 2.42(1)

[a] Space group: *Cmcm*. a = 2.9367(2) Å, b = 5.4015(5) Å, c = 10.8248(8) Å. b/a = 1.84. Absorption correction: 0.377 (λ = 0.39985 Å). R_{wp} = 8.40%; R_B = 7.13% with excluded regions (graphite).

It is noteworthy that, whereas two crystallographic sites can be occupied by the Na^+ ions in the P′2 orthorhombic structure in the *Cmcm* space group,[10] only the site sharing edges with the MO_6 octahedra is occupied here. Generally in a P2-type structure Na_e and Na_f sites are both simultaneously occupied with a ratio close to 2:1. This distribution results from the strong Na^+−Na^+ repulsion which prevails over the the Na^+−$M^{3+/4+}$ repulsion. As adjacent Na_e and Na_f sites cannot be occupied simultaneously, the stoichiometry $NaMn_{1/2}Fe_{1/2}O_2$ can only be reached if all Na^+ ions are located in one site. Therefore, the most stable site, i.e. Na_e, is occupied (Figure 9). Note also that the ADP value for the Na^+ ions in the P′2 phase is lower (0.7(2) Å^2) than that for the P2-$Na_{0.62}Mn_{1/2}Fe_{1/2}O_2$ phase (1.9(3) Å^2), in agreement with the fact that the Na^+ ions should be much less mobile for a stoichiometry close to $NaMn_{1/2}Fe_{1/2}O_2$.

Raman Spectroscopy. In order to investigate the local structure, Raman scattering experiments were performed on several $Na_xMn_{1/2}Fe_{1/2}O_2$ phases, as shown in Figure 10. Since the spectrum of the P′2-$NaMn_{1/2}Fe_{1/2}O_2$ phase is significantly different from those for the other phases, a clear change in symmetry is evidenced, in agreement with our previous results (crystal point groups as well as Na/M/O local site symmetries are distinct for the P2 and P′2 phases). Despite these distinct symmetries of P2 and P′2 phases, the shift of the P′2 spectrum to lower wavenumbers is representative of an increase of some characteristic distances in the structure. As the interslab distance decreases, Raman spectroscopy is here particularly sensitive to the MO_2 slab average deformation: the M−M average in-plane distances (Figure 7b) and the slab thicknesses (2.15(1) Å for the P′2 phase vs 2.08(1) Å for the P2-$Na_{0.62}Mn_{1/2}Fe_{1/2}O_2$ phase). The Raman sensitivity to the MO_2 slabs is reinforced by Figure S2 (Supporting Information), which shows the similarity of the Raman spectra of structures with similar MO_2 slabs but different stackings such as O3-$Na_xMn_{1/2}Fe_{1/2}O_2$ and P2-$Na_xMn_{1/2}Fe_{1/2}O_2$. Since the spectra obtained for the P2-$Na_xMn_{1/2}Fe_{1/2}O_2$ phases with x = 0.62, 0.50, and 0.40 are quite similar, one can conclude that the MO_2 slabs are maintained upon cycling, in good agreement with the XRPD data. The slight shift to higher wavenumbers observed while the Na amount is decreased reflects a strengthening of the chemical bonds, due to the increasing covalence of the M−O bonds that leads to a decrease of the slab thickness and a shortening of the M−M distances, the latter being in agreement with the XRPD data. Although the $Na_{\approx 0.15}Mn_{1/2}Fe_{1/2}O_2$ phase exhibits a different XRPD pattern, its spectrum is quite similar to those of the P2 phases, except that the bands are broadened and are clearly more shifted to higher wavenumbers. This result provides evidence of MO_2 slabs in the "Z" phase similar to those of the P2 phases with a strong shortening of some distances in the MO_2 slab. The slab thickness should be the most affected, since the evolution of the M−M average in-plane distance is rather continuous (Figure 7b). As for XRPD, the broadening of the bands indicates a strong disorder in the structure, which could be due to the presence of stacking faults.

■ CONCLUSION

The P2-$Na_xMn_{1/2}Fe_{1/2}O_2$ phase prepared by autocombustion synthesis was further investigated in this work. The SXRPD pattern of the pristine material does not show any evidence of a significant amount of transition-metal vacancies, as we previously suggested.[3d] The study of its electrochemical properties as a positive electrode material reveals interesting discharge capacities on cycling up to 4.0 V, associated with interesting capacity retention (85% after 50 cycles at C/20). We believe this result can be further improved by design and optimization of the electrode and optimization of the particle morphology. When it is cycled up to 4.3 V, the material shows drastic diminution of the discharged capacity retention down to 61%, despite a higher initial discharge capacity. The operando in situ XRPD experiment showed several reversible structural transitions upon Na deintercalation from the intercalated phase. The almost fully intercalated phase exhibits an orthorhombic distortion. The Rietveld refinement clearly shows that the cooperative Jahn−Teller effect is the driving force of this transition. A new phase with an unknown slab packing is observed at high voltage. Nevertheless, a well-crystallized phase is obtained after sodium reintercalation. This shows that the structural transitions have no important effect on the short-term cycling of the material. Studies of their effects during long-range cycling are in progress.

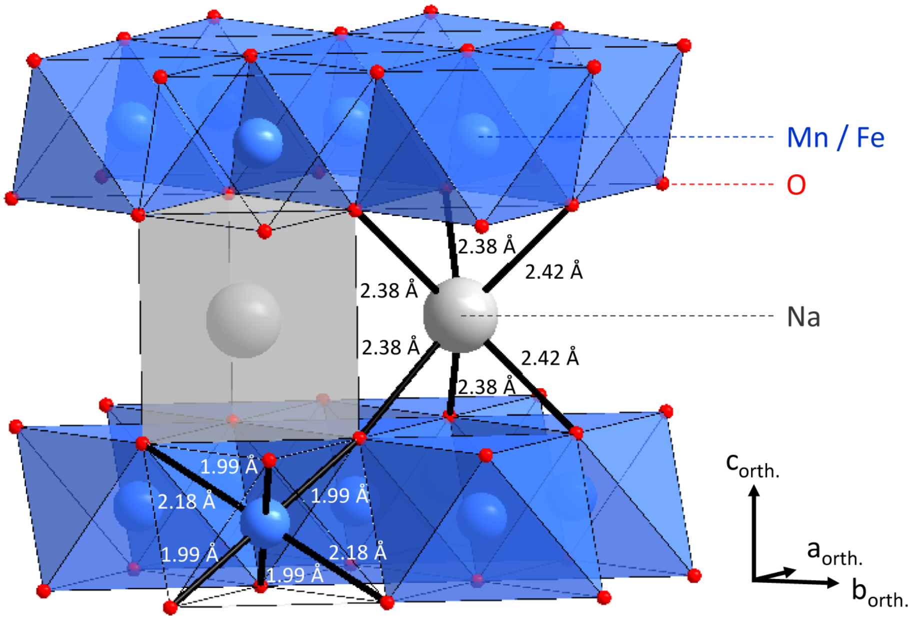

Figure 9. Representation of the MO_6 and NaO_6 polyhedra in the P′2-$NaMn_{1/2}Fe_{1/2}O_2$ phase: highlighting of the cooperative Jahn−Teller effect.

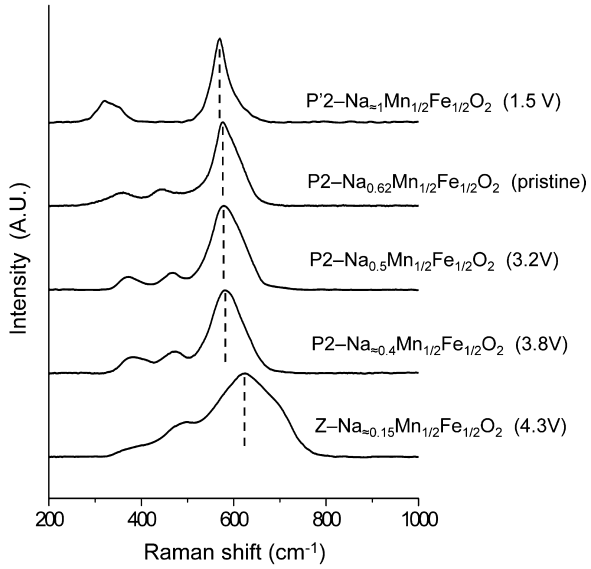

Figure 10. Raman spectra recorded ex situ for several $Na_xMn_{1/2}Fe_{1/2}O_2$ phases. The P2-$Na_{0.62}Mn_{1/2}Fe_{1/2}O_2$ phase is the pristine material, and the others are obtained by a galvanostatic charge or discharge followed by a potentiostatic step at the selected voltages indicated in parentheses.

■ ASSOCIATED CONTENT

Ⓢ Supporting Information

Figures giving an inversed representation of the in situ XRPD experiment and Raman spectra of the P2- and O3-$Na_xMn_{1/2}Fe_{1/2}O_2$ phases. This material is available free of charge via the Internet at http://pubs.acs.org.

■ AUTHOR INFORMATION

Corresponding Author

*D.C.: E-mail: carlier@icmcb-bordeaux.cnrs.fr. Tel.: +33 5 40 00 35 69.

Notes

The authors declare no competing financial interest.

■ ACKNOWLEDGMENTS

This work benefitted from a grant from the Agence Nationale de la Recherche (Blanc Inter II, SIMI 8), No. 2011-IS08-01. Region Aquitaine and CNRS are also acknowledged for a scholarship for B.M.d.B. The authors are thankful to M. R. Suchomel (APS, Argonne National Laboratory, Argonne, IL, USA) for the SXRPD pattern of the P2 pristine material and to C. Drathen for her help on the ID31 beamline (ESRF, Grenoble, France). E. Suard (ILL, Grenoble, France) is acknowledged for her help on the D2B neutron diffraction beamline. Use of the Advanced Photon Source at Argonne National Laboratory was supported by the U. S. Department of Energy, Office of Science, Office of Basic Energy Sciences, under Contract No. DE-AC02-06CH11357.

■ REFERENCES

(1) (a) Xu, J.; Lee, D. H.; Meng, Y. S. *Funct. Mater. Lett.* **2013**, *06* (01), 1330001−1. (b) Palomares, V.; Casas-Cabanas, M.; Castillo-Martínez, E.; Han, M. H.; Rojo, T. *Energy Environ. Sci.* **2013**, *6* (8), 2312−2337.

(2) (a) Yabuuchi, N.; Yoshida, H.; Komaba, S. *Electrochemistry* **2012**, *80* (10), 716−719. (b) Zhao, J.; Zhao, L.; Dimov, N.; Okada, S.; Nishida, T. *J. Electrochem. Soc.* **2013**, *160* (5), A3077−A3081.

(3) (a) Yabuuchi, N.; Kajiyama, M.; Iwatate, J.; Nishikawa, H.; Hitomi, S.; Okuyama, R.; Usui, R.; Yamada, Y.; Komaba, S. *Nat. Mater.* **2012**, *11* (6), 512−517. (b) Yoncheva, M.; Stoyanova, R.; Zhecheva, E.; Kuzmanova, E.; Sendova-Vassileva, M.; Nihtianova, D.; Carlier, D.; Guignard, M.; Delmas, C. *J. Mater. Chem.* **2012**, *22* (44), 23418−23427. (c) Thorne, J. S.; Dunlap, R. A.; Obrovac, M. N. *J. Electrochem. Soc.* **2012**, *160* (2), A361−A367. (d) Mortemard de Boisse, B.; Carlier, D.; Guignard, M.; Delmas, C. *J. Electrochem. Soc.* **2013**, *160* (4), A569−A574. (e) Singh, G.; Acebedo, B.; Cabanas, M. C.; Shanmukaraj, D.; Armand, M.; Rojo, T. *Electrochem. Commun.* **2013**, *37*, 61−63. (f) Kodera, T.; Ogihara, T. *J. Ceram. Soc. Jpn.* **2014**, *122* (6), 483−487. (g) Park, K.; Han, D.; Kim, H.; Chang, W.-s.; Choi, B.; Anass, B.; Lee, S. *R. Soc. Chem. Adv.* **2014**, *4* (43), 22798−22802. (h) Zhao, J.; Xu, J.; Lee, D. H.; Dimov, N.; Meng, Y. S.; Okada, S. *J. Power Sources* **2014**, *264*, 235−239. (i) Zhu, H.; Lee, K. T.; Hitz, G. T.; Han, X.; Li, Y.; Wan, J.; Lacey, S.; Cresce, A.; Xu, K.; Wachsman, E.; Hu, L. *ACS Appl. Mater. Interfaces* **2014**, *6* (6), 4242−4247.

(4) (a) Kim, D.; Lee, E.; Slater, M.; Lu, W.; Rood, S.; Johnson, C. S. *Electrochem. Commun.* **2012**, *18*, 66–69. (b) Yabuuchi, N.; Yano, M.; Yoshida, H.; Kuze, S.; Komaba, S. *J. Electrochem. Soc.* **2013**, *160* (5), A3131–A3137.

(5) (a) Lu, Z.; Dahn, J. R. *Chem. Mater.* **2001**, *13*, 1252–1257. (b) Sathiya, M.; Hemalatha, K.; Ramesha, K.; Tarascon, J. M.; Prakash, A. S. *Chem. Mater.* **2012**, *24* (10), 1846–1853. (c) Buchholz, D.; Moretti, A.; Kloepsch, R.; Nowak, S.; Siozios, V.; Winter, M.; Passerini, S. *Chem. Mater.* **2013**, *25* (2), 142–148. (d) Yuan, D.; He, W.; Pei, F.; Wu, F.; Wu, Y.; Qian, J.; Cao, Y.; Ai, X.; Yang, H. *J. Mater. Chem. A* **2013**, *1* (12), 3895–3899. (e) Chagas, L. G.; Buchholz, D.; Wu, L.; Vortmann, B.; Passerini, S. *J. Power Sources* **2014**, *247*, 377–383. (f) Doubaji, S.; Valvo, M.; Saadoune, I.; Dahbi, M.; Edström, K. *J. Power Sources* **2014**, *266*, 275–281.

(6) Delmas, C.; Fouassier, C.; Hagenmuller, P. *Phys. 99B* **1980**, 81–85.

(7) Komaba, S.; Ishikawa, T.; Yabuuchi, N.; Murata, W.; Ito, A.; Ohsawa, Y. *ACS Appl. Mater. Interfaces* **2011**, *3* (11), 4165–4168.

(8) Leriche, J. B.; Hamelet, S.; Shu, J.; Morcrette, M.; Masquelier, C.; Ouvrard, G.; Zerrouki, M.; Soudan, P.; Belin, S.; Elkaïm, E.; Baudelet, F. *J. Electrochem. Soc.* **2010**, *157* (5), A606–A610.

(9) (a) Bordet-Le Guenne, L.; Deniard, P.; Biensan, P.; Siret, C.; Breca, R. *J. Mater. Chem.* **2000**, *10*, 2201–2206. (b) Carlier, D.; Cheng, J. H.; Berthelot, R.; Guignard, M.; Yoncheva, M.; Stoyanova, R.; Hwang, B. J.; Delmas, C. *Dalton Trans.* **2011**, *40* (36), 9306–9312.

(10) Stoyanova, R.; Carlier, D.; Sendova-Vassileva, M.; Yoncheva, M.; Zhecheva, E.; Nihtianova, D.; Delmas, C. *J. Solid State Chem.* **2010**, *183* (6), 1372–1379.

(11) Parant, J.-P.; Olazcuaga, R.; Devalette, M.; Fouassier, C.; Hagenmuller, P. *J. Solid State Chem.* **1971**, *3*, 1–11.

(12) (a) Lu, Z.; Dahn, J. R. *J. Electrochem. Soc.* **2001**, *148* (11), A1225–A1229. (b) Mortemard de Boisse, B.; Cheng, J. H.; Carlier, D.; Pan, C. J.; Bordère, S.; Filimonov, D.; Drathen, C.; Suard, E.; Hwang, B. J.; Wattiaux, A.; Delmas, C. *Chem. Mater.* **2014**, submitted.

(13) Delmas, C.; Fouassier, C. *Z. Anorg. Allg. Chem.* **1976**, *420*, 184–192.

(14) Ma, X.; Chen, H.; Ceder, G. *J. Electrochem. Soc.* **2011**, *158* (12), A1307–A1312.